Bias field reduction by localized Lloyd–Max quantization ☆

Zhenhua Mai[a],*, Rudolf Hanel[b], Joost Batenburg[a], Marleen Verhoye[c],
Paul Scheunders[a], Jan Sijbers[a]

[a]*IBBT-VisionLab, Department of Physics, Universiteit Antwerpen, Wilrijk, 2610 Antwerp, Belgium*
[b]*Complex Systems Research Group, Medical University of Vienna, 1090 Vienna, Austria*
[c]*Bio-Imaging Lab, Biomedical Department, Universiteit Antwerpen, Wilrijk, 2610 Antwerp, Belgium*

Abstract

Bias field reduction is a common problem in medical imaging. A bias field usually manifests itself as a smooth intensity variation across the image. The resulting image inhomogeneity is a severe problem for posterior image processing and analysis techniques such as registration or segmentation. In this article, we present a novel debiasing technique based on localized Lloyd–Max quantization (LMQ). The local bias is modeled as a multiplicative field and is assumed to be slowly varying. The method is based on the assumption that the global, undegraded histogram is characterized by a limited number of gray values. The goal is then to find the discrete intensity values such that spreading those values according to the *local* bias field reproduces the *global* histogram as good as possible. We show that our method is capable of efficiently reducing (even strong) bias fields in 3D volumes.
© 2011 Elsevier Inc. All rights reserved.

Keywords: Bias field; Lloyd–Max quantization; Debiasing C-means

1. Introduction

Medical image data often suffer from intensity inhomogeneities (bias fields). In magnetic resonance imaging (MRI), this artifact may have several causes, such as a lack of uniform sensitivity of the RF-emitting and -receiving coils, static field (B_0) inhomogeneities, gradient-induced eddy currents, magnetic susceptibility of tissue, interslice cross-talk, RF standing wave effects and attenuation of the RF signal inside the object [1,2].

A bias field usually manifests itself as a smooth intensity variation across the image. Automated extraction of useful information from images demands an automated detection and correction of the bias field. Indeed, tasks like image quantization, segmentation [3] or tissue classification can be severely impeded by degraded intensity homogeneities of images. For example, Kohn et al. [3] observed that a bias field elongates the clusters that represent the brain and cerebrospinal fluid such that the segmentation of the gray and white matter is severely affected.

Various methods have been proposed in order to reduce an image bias field, with different degrees of success. A recent review on methods for correction of intensity inhomogeneities has been written by Vovk et al. [4]. According to their work, current bias field reduction methods can be subdivided as follows:

- **Filtering methods:** Low-pass filtering methods assume that the intensity inhomogeneity corrupting the image is a low-frequency signal component that can be separated from the high-frequency information of the imaged anatomical structures. However, this assumption is only accurate if the imaged anatomical structures are relatively small and hence contain no low frequencies that might be mistakenly removed by low-pass filtering. For most of the anatomical structures imaged by an MR scanner this assumption does not hold, which results in overlap of anatomy and inhomogeneity frequency spectra, thereby limiting the feasibility of filtering methods. Homomorphic filtering

and homomorphic unsharp masking have been proposed. Morphological filtering [5] and simple high-pass filtering belong to this group of methods but have not shown to be useful for MRI.

- **Surface fitting methods:** These methods fit a parametric surface to a set of image features (intensity or gradient based) that contain information on intensity inhomogeneity. The resulting surface, which is usually polynomial or spline based, represents the multiplicative inhomogeneity field that is used to correct the input image [6,7].
- **Segmentation-based methods:** It is well known that images that need to be segmented in homogeneous regions require preprocessing to remove the bias field prior to segmentation. In turn, removal of the bias field in an image becomes trivial when the image is subdivided into classes that should be homogeneous. Methods were proposed that exploit this duality based on maximum likelihood, expectation maximization [8,9] and fuzzy C-means clustering [10,11], and often solved by means of functional minimization.

Based on the categorization of Vovk et al. [4], the method we will present is novel to the best of our knowledge and is likely to be situated in the category *segmentation*-based methods. However, the functional that we will consider for minimization is not entropy related [12] but a measure simply based on the mean squared error (MSE) [11].

Segmentation and tissue classification are problems that are related to the field of image quantization. Where segmentation tries to classify the image domain into distinct regions that meet some criterion (being an element in some threshold interval, in its simplest form), tissue classification tries to label each pixel of the image domain by one or more tissue indices. Image quantization (Lloyd–Max, C-means quantization) [13] on the other hand tries to find a reduced set of intensity values that allows to represent a large number of gray values in an optimal way, which is usually provided by MSE measures.

In this article, we show how a local Lloyd–Max quantization (LMQ) approach can be effectively used to debias medical images. No presmoothing scheme is required, as our method works still rather well in situations with heavy noise. We will also show that the proposed method is very well capable of significantly reducing strong bias fields in simulated as well as real 3D medical data sets.

The article is organized as follows: First we start with a general description of the inspiration for our bias field reduction approach. Next, a formulation of the image model is presented. In Subsection 2.2 to 2.3, the well-known LMQ procedure (without bias field) is briefly summarized and then extended to image models that contain bias fields, after which the algorithm schemes are introduced in sections. In Section 3, various experiments to test the debiasing performance of the proposed method are conducted and discussed. Finally, in Section 4, we draw the conclusions.

2. Method

2.1. Inspiration

In this article, the model we employed for the undegraded image (i.e., no bias field or noise) assumes that the image can be subdivided into a fixed number of classes, where image intensities inside each class are distinct from those of the others. This implies that the undegraded image can be segmented into distinct parts, each of which can be classified with a characteristic gray level. For example, an MR image of the brain can be modeled to consist of four classes: background, cerebrospinal fluid, gray matter and white matter. For such an image model, the global histogram of the undegraded image will contain only a limited number of peaks. However, if the undegraded image is polluted by a bias field or noise, the global image histogram will be smoothed out and/or expanded, thereby making the sharp peaks indistinct.

The effect of noise and bias on the intensity distribution is demonstrated in Figs. 1 and 2. Fig. 1(A) shows the Shepp–Logan phantom (SLP), which consists of only a small fixed number of pixel classes. The global histogram, shown in Fig. 1 (D), shows clear peaks for each gray value in the image. In Fig. 1(B) and (C), the undegraded image of Fig. 1(A) is polluted with noise and a multiplicative bias field, respectively. As can be seen from the corresponding histograms, shown in Fig. 1(E) and (F), respectively, when noise or bias degradation is sufficiently strong, information about the position of the discrete intensity values of the undegraded image is lost in the *global* histogram. Moreover, the broadened and/or shifted histogram curves make it almost impossible to locate the original sharp peaks. However, in comparison, the *local* histogram better retains this information. For example, Fig. 2 (A) and (C) shows two local areas extracted from the red square and blue square of Fig. 1(C). From their respective histograms in Fig. 2(B) and (D), we can see that the local peaks are much thinner and the difference in peak positions is due to the multiplicative bias field. Therefore, the *local* bias field can be obtained, if the original distinct peaks' positions are known. However, real-life image debiasing tasks often come with no prior knowledge about the original characteristic gray levels except their number (as assumed in our model). This observation inspired us to combine the *local* bias field recovery with a global image quantizer, iteratively, to obtain the *global* bias field, as detailed below.

2.2. Image model and LMQ

Our original undegraded (i.e., without bias field or noise) image X_k is defined on a 3-D domain $\Omega=\{(i,j,l)|0 \le i \le I_{max}, 0 \le j \le J_{max}, 0 \le l \le L_{max}\}$, with $0 \le X_k \le X_{max}$, where k indicates the kth voxel and X_{max} is the maximum image intensity.

The multiplicative bias field B_k is defined on the same domain Ω. With bias field, the degraded image will then be

$$Y_k = X_k \times B_k + n_k \tag{1}$$

where n_k indicates the additive noise.

A The original SLP

B The SLP with noise

C The SLP with a bias field

D The histogram for the original SLP

E The histogram for the SLP with noise

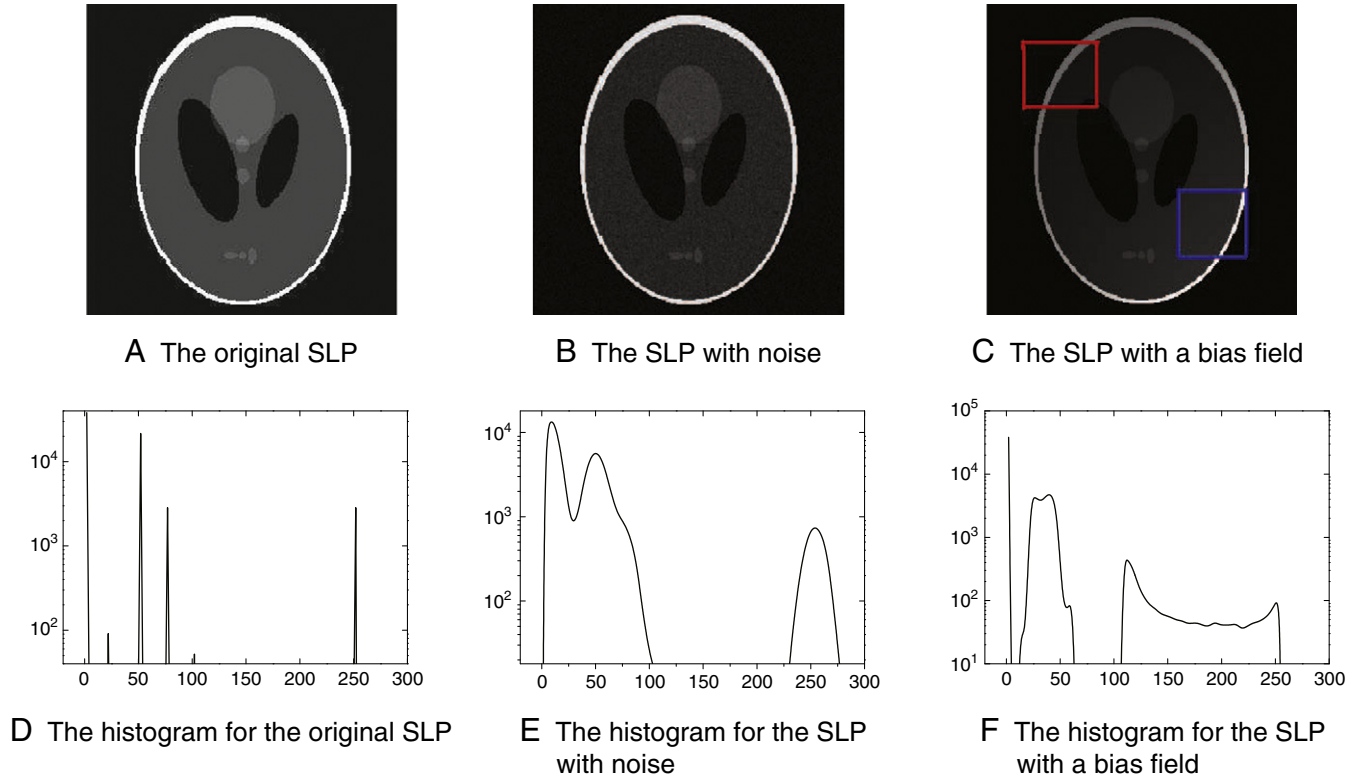F The histogram for the SLP with a bias field

Fig. 1. The effect of noise and bias on the global intensity histogram (histograms in logarithmic scale) using the SLP as an example. From left to right, SLP with no noise, 40% noise and a linear intensity bias in both the *x*-direction and *y*-direction. The order of the histograms in the bottom is the same. The red and blue square indicate the extracted subregions to be shown in Fig. 2.

The undegraded image can be effectively quantized using LMQ. Let $Q \equiv \{q_i\}_{i=1}^{N}$ denote the set of characteristic gray levels after quantization and $\rho(X)$ the discrete global histogram of the image to be quantized. The optimal quantization is obtained when the total MSE, given by

$$\sigma^2 = \sum_{i=1}^{N} \sum_{X=t_{i-1}}^{t_i} \rho(X)(X-q_i)^2, \tag{2}$$

is minimal with respect to quantized levels $\{q_i\}$. $T \equiv \{t_{i-1}\}_{i=1}^{N}$ is the set of threshold values associated with each level, with $q_i \in (t_{i-1}, t_i)$. Minimization of σ^2 with respect to the parameter sets Q and T (by differentiating σ^2 with respect to t_i and q_i) leads to the following set of conditions:

$$t_i = \frac{1}{2}(q_{i+1} + q_i), \quad \text{with } i = 0,\ldots,N-1 \tag{3}$$

$$q_i = Z_i^{-1} \sum_{X=t_{i-1}}^{t_i} \rho(X)X, \quad \text{with } i = 1,\ldots,N \tag{4}$$

where

$$Z_i = \sum_{X=t_{i-1}}^{t_i} \rho(X), \quad \text{with } i = 1,\ldots,N \tag{5}$$

With Eqs. (3) to (5), it is then possible to iteratively calculate σ^2 until convergence is reached, thereby obtaining the optimal Q and T.

2.3. Bias field estimation with LMQ

In the previous section, we have used the Lloyd–Max method to quantize the undegraded image with a number of characteristic gray levels, which, however, will be distorted by the presence of bias field in the degraded image. Nevertheless, the bias field estimation can still benefit from the LMQ, albeit in a modified form. Recall from Subsection 2.1 that the bias field recovery is more effective in a local region than on the global image. Therefore, we first divide the global image into P subdivisions:

$$\{D_p | D_p \subset \Omega, \ 1 \leq p \leq P\} \tag{6}$$

The subdivisions $\{D_p\}$ have to satisfy

$$\bigcup_{p=1}^{P} D_p = \Omega$$

From Eq. (1), for each subdivision D_p, we have

$$X_k \cong Y_k / B_k|_{k \in D_p}$$

A The subregion for red square area

B The histogram for the red square area

C The subregion for blue square area

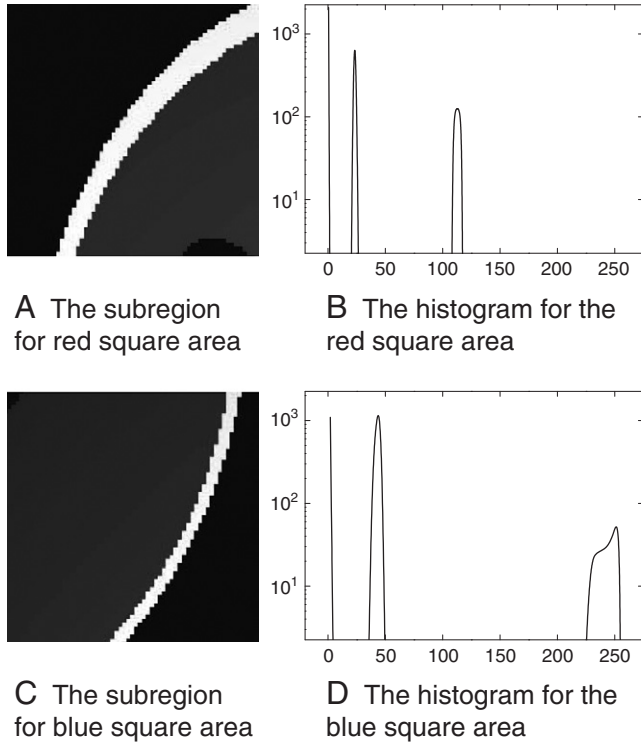**D** The histogram for the blue square area

Fig. 2. The effect of noise and bias on the local intensity histogram (histograms in logarithmic scale) using the SLP as an example. Top figure is from the red square subregion in Fig. 1 and the bottom from the blue square. Histograms follow the same order.

Similar to Eq. (2), we have

$$\sigma^2 = \sum_{D_p} \sigma_{D_p}^2 = \sum_{D_p} \sum_{k \in D_p} \sum_{i=1}^{N} \sum_{Y_k = t_{i-1}}^{t_i} \rho_k(Y_k) \left(\frac{Y_k}{B_k} - q_i \right)^2. \quad (7)$$

After differentiation of σ^2 with respect to B, Q and T, we have

$$B_k = \frac{\sum_{i=1}^{N} \sum_{Y_k = t_{i-1}}^{t_i} \rho_k(Y_k)(Y_k)^2}{\sum_{i=1}^{N} q_i \sum_{Y_k = t_{i-1}}^{t_i} \rho_k(Y_k) Y_k}, \quad \text{with } k \in D_p \quad (8)$$

$$q_i = \frac{\sum_{D_p} \sum_{k \in D_p} \frac{1}{B_k} \sum_{Y_k = t_{i-1}}^{t_i} \rho_k(Y_k) Y_k}{\sum_{D_p} \sum_{k \in D_p} \sum_{Y_k = t_{i-1}}^{t_i} \rho_k(Y_k)}, \quad \text{with } i = 1, ..., N \quad (9)$$

$$t_i = \frac{1}{2} (q_{i+1} + q_i) \frac{\sum_{D_p} \sum_{k \in D_p} \rho_k(t_i)}{\sum_{D_p} \sum_{k \in D_p} \rho_k(t_i) \frac{1}{B_k}}, \quad \text{with } i = 0, ..., N-1 \quad (10)$$

It is obvious that bias field is only fixed up to a global factor, so we impose the additional constraint for a normalized bias field, namely:

$$\sum_{D_p} \sum_{k \in D_p} \rho_k(t_i) = \sum_{D_p} \sum_{k \in D_p} \rho_k(t_i) \frac{1}{B_k} \quad (11)$$

So, after inserting the relation in Eq. (11), Eq. (10) reduces to Eq. (3).

Similar to a classic Lloyd–Max problem, Eqs. (8)–(10) have to be solved in an iterative manner. Afterwards, the local bias fields will have to be pieced together to obtain the final global bias field, the details for which will be given below.

2.4. From the local bias field to the global one

Obtaining optimal solutions from Eqs. (7) to (10) relies not only on an optimal iterative minimizing scheme, but also on the setup of the subdivisions $\{D_p\}$. The first issue is the definition of "local," or in other words, how do we suppose the bias field behaves in a small scale? Typically, the bias field is assumed to be smoothly varying and therefore can be approximated by a piecewise constant field. While the "piece" (subdivisions) should be small enough to reflect the locality of the bias field, we should also ensure that its dimensions allow for enough (statistical) information to support any valid analysis. Presently, the piecewise constant field will be further smoothed and interpolated into a pixelated field that better approximates the true bias field. The second issue is the overlapping between subdivisions. The theorizing in the previous section says nothing about the method to generate the subdivisions, and Eqs. (7) to (10) do not impose any overlapping constraint (*local* information sharing) across individual subdivisions. However, since the bias field is only fixed up to a factor, a set of minimizers for the local optimization (local bias fields) put together does not necessarily represent the global minimizer (global bias field), and especially not if the local optimizations are done separately. Therefore, finding ways to channel information between subdivisions becomes mandatory. We can impose subdivisions to be physically overlapping with each other (physical overlap scheme, POS); alternatively, we can provide certain information-sharing mechanism for nonoverlapping subdivisions (virtual overlap scheme, VOS). The rest of this section will introduce both mechanisms and the associated minimization process.

2.4.1. Physical overlapping scheme

In the POS, the subdivisions are generated such that each subdivision D_p always has physical overlappings with its neighbors.
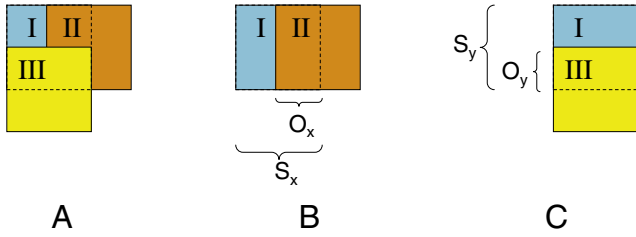
Fig. 3. An example of the physical overlapping subdivisions in POS. Subdivision I (dash line) has 50% overlapping with Subdivisions II and III, as decomposed in (B) and (C) respectively. S_x and S_y indicate the size of subdivisions in the x and y directions, while O_x and O_y represent the degrees of overlappings in each direction.

For example, a typical setup can be like that shown in Fig. 3, with

$$D_I = \{(x,y,z) \mid m \leq x \leq m + S_x, \ j \leq y \leq j + S_y, \ l \leq z \leq + S_z\}$$
$$D_{II} = \{(x,y,z) \mid m + O_x \leq x \leq m + S_x + O_x, \ j \leq y \leq j + S_y, \ l \leq z \leq + S_z\}$$
$$D_{III} = \{(x,y,z) \mid m \leq x \leq m + S_x, \ j + O_y \leq y \leq j + S_y + O_y, \ l \leq z \leq + S_z\}$$

where S_x, S_y and S_z are the subdivision dimensions, and O_x, O_y and O_z control the degree of overlappings. In practice, we can just set $O_i = \frac{1}{2}S_i$ ($i=x,y,z$), so that each subdivision will have 50% overlapping with each of its neighbors.

In POS, the local bias field B_k is taken to be constant inside each subdivision D_p, whose bias field value will be denoted as B_p. We use a simulated annealing technique to solve the minimization problem. Roughly put, the MSE σ_p^2 for D_p is calculated according to Eq. (7), with an initial estimate of the bias field $\{B_p\}$, and then the overall MSE $\sum_p \sigma_p^2$ is iteratively minimized with a randomly varied bias field $\{B_p\}$, until the preset convergence thresholds are reached. T and Q are also updated in each iteration accordingly. The pseudo-code for this process is shown in Fig. 4.

After the local bias fields B_p are obtained, the global bias field B_k can be approximated using a bi-linear interpolation. It is obvious that the dimension of subdivisions directly influences how accurately the interpolated $\tilde{B}_k$ reflects the true bias field B_k. For example, subdivisions of half the overall image's dimension will be unlikely to represent the local variation of the global bias field of, e.g., about 1/10th of the image scale. However, it is equally unwise to use subdivisions down to very small dimensions, e.g., about a few voxels in each dimension. The reason is rooted in the fact that the whole LMQ framework is a statistical method, which relies on a sufficient number of samples to carry out any meaningful statistical analysis. Therefore, for robustness and stability, the subdivision dimension in POS is set to be at least one-eighth of the image dimension.

2.4.2. Virtual overlapping scheme

In VOS, subdivisions are generated without physical overlappings with each other. However, as mentioned earlier, certain information channeling between subdivisions must be provided. In VOS, we utilize a multi-resolution approach to facilitate an optimum search, as is shown in

Fig. 5. Firstly, a subdivision D_p is further divided into M smaller sub-blocks, with local bias field B_k assumed to be constant only in those sub-blocks (instead of constant in the whole subdivision in POS), denoted as B_p^m, and then a virtual subdivision is formed from adjacent sub-blocks of neighbor subdivisions. Afterwards, optimizations of MSE with respect to $\{B_p^m\}$ are carried out first on all physical subdivisions and then on the virtual one. The optimized result from the virtual subdivision is used to update the results for all physical subdivisions so that the separate optimizations in local regions can properly represent the global bias field. For example, as shown in Fig. 5, suppose, after optimization, that the optimal local bias field inside Subdivision 1 is

$$1 : \{a, b, c, d\}$$

where the last value corresponds to the bottom right sub-block of Subdivision 1, while the optimal results for Subdivision 5 is

$$5 : \{e, f, g, h\}$$

where the first value corresponds to the upper left sub-block of Subdivision 5, same as the bottom right block of Subdivision 1, then the updated results for Subdivision 1 will be

$$1 : \left\{\frac{e}{d}a, \frac{e}{d}b, \frac{e}{d}c, e\right\}$$

The results of Subdivisions 2, 3 and 4 are similarly updated. This update method is plausible simply because of the multiplicative nature of the bias field, which remains

---

Initialize :
    Initialize all the local bias fields B_p to be unity, $B_p = 1$
    Initialize Q and T
    Initialize randomizer a and convergence thresholds TH_1 and TH_2
do
{
    Calculate Q and T with Eqs. 9-10
    do
    {
        Calculate MSE σ_p^2 for all subdivisions and total MSE $\sigma^2 = \sum_p \sigma_p^2$

        for each subdivision D_p:
            test a new random bias field value $B_p^* = B_p \times a, \ a > 0$
            calculate the new MSE σ_p^{2*}
            if $\sigma_p^{2*} < \sigma_p^2$
                $B_p = B_p^*, \ \sigma_p^2 = \sigma_p^{2*}$

        $\sigma^{2*} = \sum_p \sigma_p^2$

    } while ($\sigma^2 - \sigma^{2*} \geq TH_1$)
    Calculate Q^* and T^*
} while ($|Q - Q^*| \geq TH_2$)
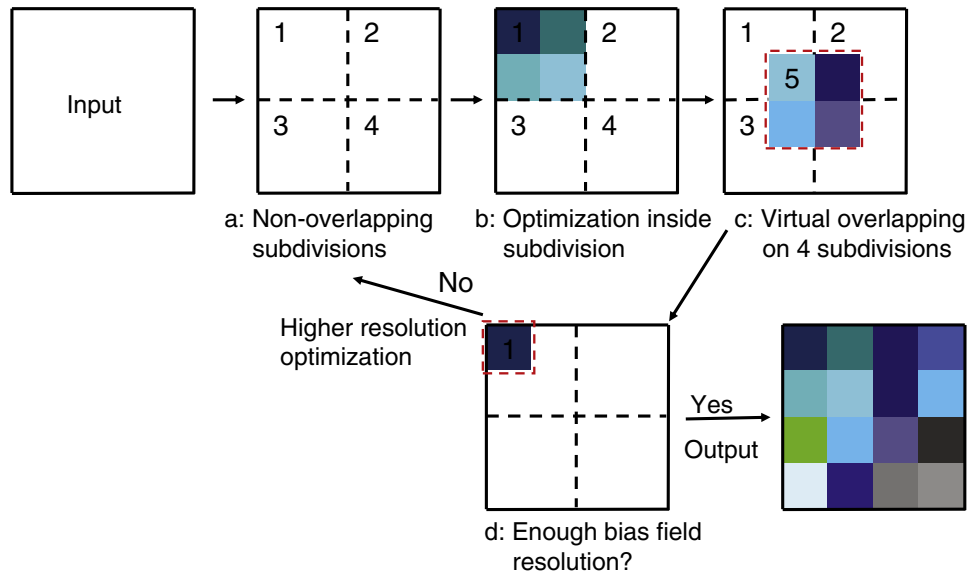Output B_p

Fig. 4. The pseudo-code for POS.

Fig. 5. The minimization process for VOS. In this 2D example, the input image is first divided into four subdivisions. Each subdivision is further divided into four smaller sub-blocks, on which the bias field is assumed to be constant, as indicated by the color block in (B). After the minimizations are carried out on each subdivision, a virtual subdivision [red dash line in (C), Subdivision 5] is formed from the adjacent sub-blocks of the four neighbor subdivisions. Similar optimization is performed on this virtual subdivision, and the result will be used to update the corresponding bias field values in the four "real" subdivisions. Then, if the sub-blocks represent a satisfactory resolution for bias field, the bias field will be output, or if not, then the sub-blocks will be treated as new subdivisions, in a higher resolution, to continue a new round of optimizations. This iterates until the required or satisfactory resolution is reached.

constant up to a nonzero factor. Furthermore, after this round of optimizations, the smaller sub-blocks inside subdivisions can be regarded as new subdivisions in a higher resolution (provided their dimension still ensures to retain enough statistical information for analyzing). Those new subdivisions can still be further divided into smaller sub-blocks, upon which one can perform a new round of optimizations. The primary advantage of VOS lies in the fact that each optimization only involves a subdivision, with $M\{B_p^m\}$ values as parameters (four in the 2D case, eight in the 3D case), instead of having to cope with the huge amount of parameters in POS (where a modest subdivision dimension of one-sixth of the image scale would result in about 1700 parameters to optimize against simultaneously). In light of this, in order to speed up the optimizations, one can use a gradient-descent search algorithm (L-BFGS [14]): the gradient of the MSE σ_p^2 for subdivision D_p with respect to

its internal local bias fields $\{B_p^m\}$ is computed and is used to guide the optimization towards the minimizer. However, it should be noted that, similar to its application elsewhere, the gradient-descent algorithm we employed is sensitive to the initial input and hence liable to be stuck in a local minimum. Nevertheless, the multi-resolution approach is a good way to help reach the global minimum. Additionally, our experiments have indicated that the output of POS can be a good initial input for VOS. Therefore, we link VOS to POS downstream in the processing pipeline.

3. Results and discussions

In this section, we present the results from various experiments where we applied our method on phantom geometric images, simulated brain images as well as real brain images.
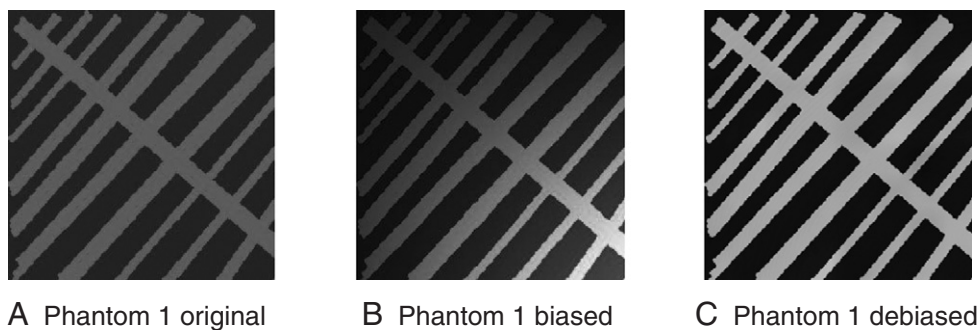

A Phantom 1 original   **B** Phantom 1 biased   **C** Phantom 1 debiased

Fig. 6. Sample result of the proposed LMQ method applied to phantom images. (A) is the original image, (B) the biased image, (C) the debiased image.
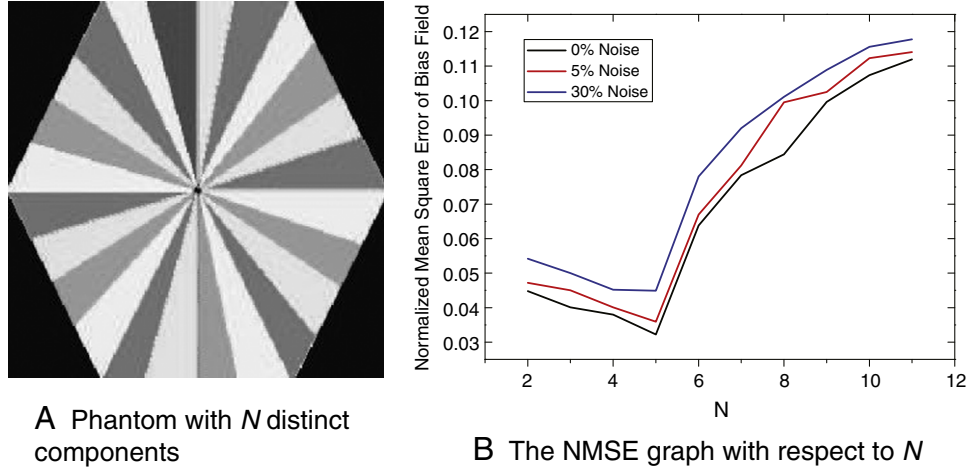
A Phantom with *N* distinct components

B The NMSE graph with respect to *N*

Fig. 7. The effect of different *N*, number of $\{q_i\}$, on the algorithm. It was tested on Phantom 2 (A), with ground truth *N*=5, on three different Rician noise levels; black line for 0% noise, red for 5% noise and blue for 30% noise.

According to Vovk et al. [4], the nonparametric nonuniformity normalization (N3) method, described in Ref. [15], has become the standard method against which other debiasing methods are compared. Hence, during the tests for simulated data and real data, we have compared our proposed LMQ algorithm to the N3 method, which is available from http://packages.bic.mni.mcgill.ca/ubuntu-intrepid/.

3.1. Phantom geometric images

Phantom geometric images consisting of a finite number of pixel classes (Figs. 6(A) and 7(A)) have been produced in order to verify the accuracy of our bias field estimation. For instance, in Fig. 6, 6(A) was polluted with a bias field lineally increasing in both the *x*- and *y*-axis, as shown in Fig. 6(B). From the debiased images, for example, Fig. 6(C), we can see that the bias field is effectively reduced. In order to compare the estimated bias field to the ground truth in a quantitative manner, we measured the normalized mean square errors (NMSE) of the estimated result from the ground truth, which is calculated as follows:

$$\text{NMSE}^{\text{LMQ}} = \sum_{i=1}^{\text{NoV}} \frac{\left(\alpha \cdot B_i^{\text{LMQ}} - B_i^{\text{GT}} \right)^2}{\text{NoV}}$$

where NoV is the number of voxels in the image; B_i^{LMQ} and B_i^{GT} are the bias fields estimated with our LMQ method and the ground truth bias field, respectively; and $\alpha = \overline{B^{\text{GT}}} / \overline{B^{\text{LMQ}}}$, with $\overline{B^{\text{GT}}}$ and $\overline{B^{\text{LMQ}}}$ being the mean values of the ground truth bias field and the estimated bias field, respectively. The NMSE results for the phantom geometric images are shown in the phantom part of Table 1.

Additionally, we tested our algorithm against different levels of noise presence in the image, which can be seen in the phantom part of Table 1. The noise we applied is of a Rician distribution, with its standard deviation increasing from 0% to 50% of the mean intensity of the original image

[16]. It can be seen that despite the presence of mild to heavy noise, our algorithm is still able to significantly reduce the bias field.

Our LMQ-based method assumes no prior knowledge of the untainted image except that it contains *N* classes of pixels. Therefore, this parameter is an integral part of the algorithm and the algorithm is sensitive to this piece of prior information. We performed a series of tests with different *N* as parameter on Phantom 2, for which the ground truth *N* is 5, and the result is shown in Fig. 7. Clearly, the algorithm performs best when the correct *N* is used; however, it is also interesting to note that the NMSE curve of the estimated bias field plateaus when *N* increases. This is largely due to the quantization nature that underlies our algorithm: its ultimate goal is to transform the histogram (debiasing) and group the intensities (quantization) into as many peaks as indicated by *N*; when *N* is sufficiently large, it would result in more quantization than debiasing. For an extreme example, if we apply the LMQ algorithm with *N* equal to the number of pixel values in a biased image, the algorithm would actually consider the biased state as the optimal result after optimization and therefore would do no debiasing at all. This observation emphasizes the importance of using the right *N*. However, on the other hand, it should also be pointed out that the impact of *N* is more immediate and stronger on the

Table 1
The NMSE of the estimated bias fields for different phantoms and synthetic brain image with respect to noise level

Noise	Phantom 1	Phantom 2	Simulated image (SI)	N3 on SI
0%	2.18E−4	12.4E−4	10.2E−4	39.8E−4
10%	3.13E−4	17.8E−4	12.7E−4	4.12E−4
30%	4.39E−4	20.5E−4	14.3E−4	45.0E−4
50%	10.8E−4	28.5E−4	16.6E−4	51.0E−4

The last column is the corresponding result from the N3 method applied to the same simulated image as in the second to the last column.
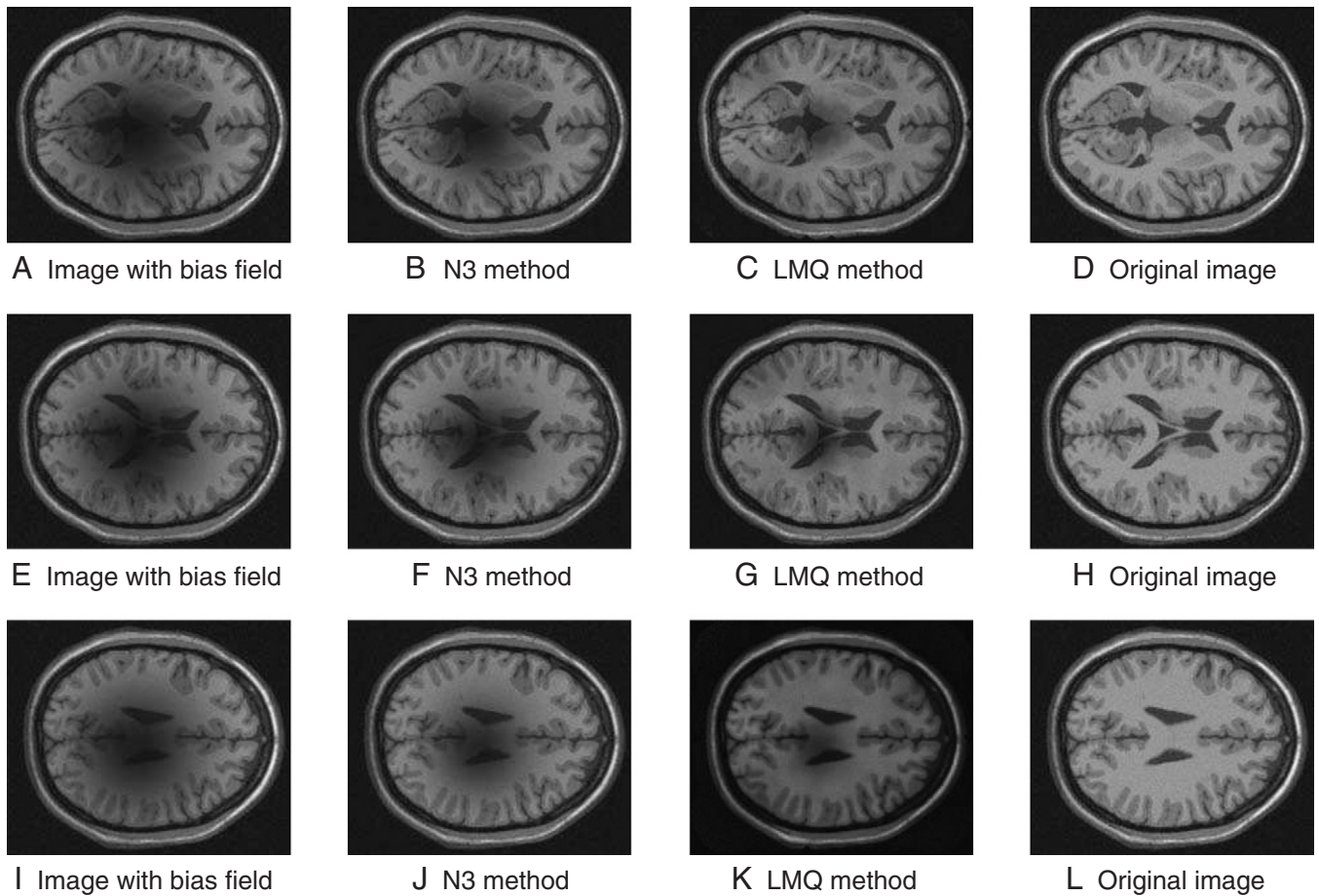
Fig. 8. Comparison between the N3 debiasing method and the proposed LMQ method with simulated images.

simple phantom geometric images, while for more realistic images our algorithm can still produce rather satisfactory results with a small deviation from the real N (see below).

3.2. Simulated image

For the test shown in Fig. 8, a pre-generated simulated brain image [17] of size 256×256×181 was used, with 3% noise. Three slices from this dataset are shown in Fig. 8(D), (H) and (L). Next, the simulated brain image was polluted with a 3D Gaussian bias field (see Fig. 8(A), (E) and (I)). Then, this image was debiased with the N3 method and the proposed LMQ method.

The results can be seen in, for example, Fig. 8(B) (for the N3 method) and (C) (for the LMQ method), respectively. From Fig. 8(B), it is clear that the N3 method reduces the bias field. The bias field reduction from our LMQ method (Fig. 8(C), (G) and (K)), however, is even more pronounced in comparison. Further quantitative NMSE result for simulated data can be seen in the simulated part of Table 1. It is clear that our method is effective in reducing bias field for simulated images that approximate real data in terms of complexity, despite the presence of heavy noise.

3.3. Real image

Finally, to prove our method's viability against real data, we also tested it on real MR images. Sample axial slices from the real data volume (256×256×256) can be seen in Fig. 9(A). Fig. 9(A) is clearly polluted by a heavy intensity inhomogeneity field, especially along the vertical direction, and, consequently, a large portion of the bottom part is obscured. Furthermore, as can be seen from the corresponding histogram in Fig. 9(C), the gray levels are almost evenly spread out. Consequently, it is likely that distinct anatomical structures will be confused during segmentation. As a result after applying our algorithm, as shown in Fig. 9(B), image intensity homogeneity is largely restored, and many previously unseen details are now clearly visible, making it suitable for further intensity-based processing. Moreover, from the comparison between the histograms of biased and debiased image in Fig. 9(C), it is shown that, in accordance with our objective to match the image histogram towards a finite set of gray level classes, not only is the histogram of the debiased image shrunken, but it is also grouped into N peaks (four in this example, including background) towards which the debiased gray levels converge. However, it is also

A Original image   **B** Debiased image   **C** Image histogram
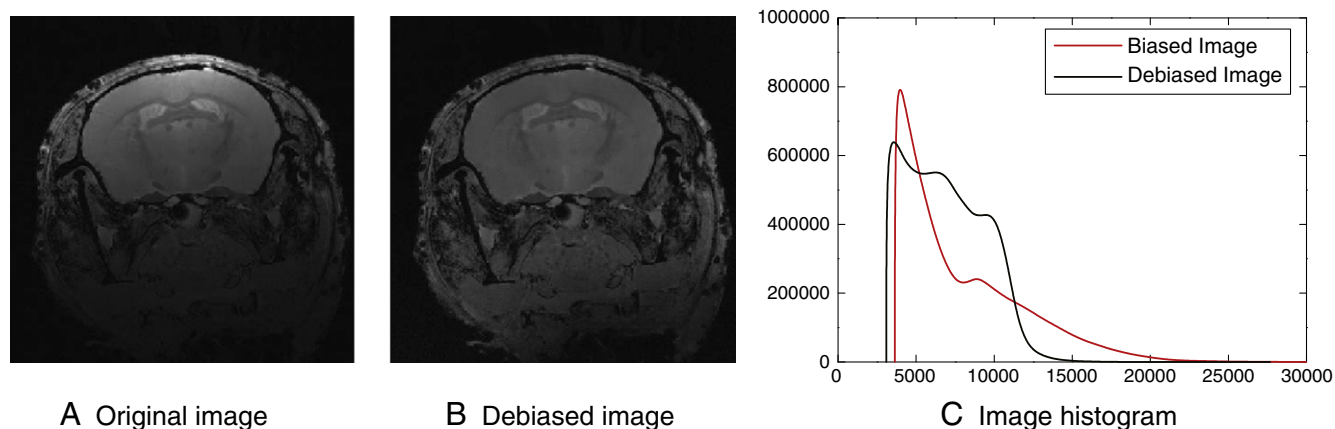
Fig. 9. Sample result of the proposed LMQ method applied to real MR images. Left image is one slice from the biased volume, the middle one is one slice from the debiased volume image and the right one is the histograms (partial, background excluded) for both volumes (red line for biased image, black line for debiased one using our method).

obvious that the convergence towards the peaks is not complete, leaving room for improvement.

We also tested the algorithm's performance on real data with respect to N. Our debiasing algorithm was applied in repetitions to a real data volume (196×256×128), and during each run we set the N to different values, ranging from 2 to 30. The sample results are shown in Fig. 10, where the leftmost image is the biased image; the second from the left is the debiased image with correct N (=4); the third and the fourth are those debiased with N=2 and 30, respectively; and the last one is debiased with the N3 method. Similarly to the previous phantom tests, when N deviates from the correct one far enough, the debiasing effect would get less and less prominent, while, on the other hand, a small deviation of N (e.g., N=2) does not result in a truly objectively inferior debiased image (subjective quantitative comparison unavailable due to the unavailability of the ground truth in the case of real data). Recall from the result for the phantom geometric images that setting N=10 will already cause the bias field

estimation to have a big error margin. Here for the real data test, the impact of erroneous N would not become manifest until it reaches as high as 25. The absence of ground truth makes a quantitative analysis difficult. Nevertheless, visual inspection from our tests suggests that, in the case of not knowing the number of voxel classes a priori, our algorithm is still capable of removing the bias field. On the other hand, this suggests a possible algorithmic extension that the parameter N might be optimized along with other variables.

Lastly, we would like to mention briefly the execution time of the algorithm. For a typical 256×256×256 MR brain data set, the computation takes approximately 50 s on a PC with Intel Pentium IV 3.0 GHz and 2 GB of memory.

4. Conclusion

In this article, we have proposed a general debiasing method based on LMQ. Our method assumes the imaged structures to consist of distinct components, which is largely
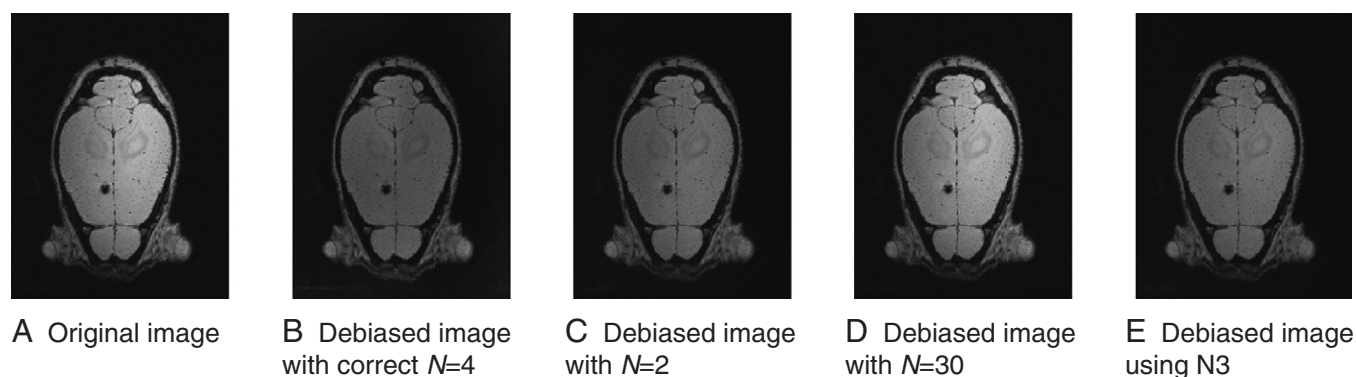

A Original image   **B** Debiased image with correct N=4   **C** Debiased image with N=2   **D** Debiased image with N=30   **E** Debiased image using N3

Fig. 10. A comparison of the choice of N on the debiasing effect. Leftmost column are the original biased images; the second column the debiased images with the correct N=4; the third and the fourth columns the debiased images with N=2 and N=30, respectively; and the final column the debiased results using the N3 method.

justifiable in anatomical scans. Apart from that, our method does not assume any prior knowledge about the bias field and is practically robust against either phantom, simulated or real images. Both simulation image and real image results showed that the LMQ bias reduction is significantly better than the commonly used N3 method. The additional noise tests as well as the real data results confirm our method's applicability to biased images heavily tainted with noise.

For future investigations, firstly, our algorithm's advantage lies in the fact that it does not assume the bias field to be following a certain (parametric) model; however, the assumption about the voxel intensity classes, namely, N, can indeed hamper its performance if prior knowledge about it is not available. Therefore, it would be interesting if we can automatize the estimation of N as part of the optimization. Secondly, the multilevel optimization is indeed efficient, yet it does not differentiate between areas of relatively denser bias field change, a consequence of which would lead to an oversmoothed bias field in an area where higher precision in the bias field is needed. This issue could be overcome by adding a locally adaptive multi-resolution approach in the VOS step of the bias field estimation.

References

[1] Simmons A, Tofts P, Barker GJ, Arridge SR. Sources of intensity nonuniformity in spin echo images at 1.5 T. Magn Reson Med 1994;32:121–8.

[2] Sled JG, Pike GB. Standing-wave and RF penetration artifacts caused by elliptic geometry: an electrodynamic analysis of MRI. IEEE Trans Med Imaging 1998;17(4):653–62.

[3] Kohn MI, Herman NK, Resnick SM, Mozley PD, Gur RE, Alavi A, et al. Analysis of brain and cerebrospinal fluid volumes with MR imaging: Part I. Methods, reliability, and validation. Radiology 2001;178:115–22.

[4] Vovk U, Pernus F, Likar B. A review of methods for correction of intensity inhomogeneity in MRI. IEEE Trans Med Imaging 2007;26 (3):405–21.

[5] Williams DB, Madisetti V. Digital signal processing handbook. Boca Raton (FL): CRC Press; 1999.

[6] Dawant BM, Zijdenbos AP, Margolin R. Correction of intensity variations in MR images for computer-aided tissues classification. IEEE Trans Med Imaging 1993;12:770–81.

[7] Milles J, Zhu YM, Gimenez G, Guttmann CR, Magnin IE. MRI intensity non-uniformity correction using simultaneously spatial and gray-level histogram information. Comput Med Imaging Graph 2007 Mar;31(2):81–90.

[8] Van Leemput K, Maes F, Vandermeulen D, Suetens P. Automated model-based bias field correction of MR images of the brain. IEEE Trans Med Imaging 1999;18:885–96.

[9] Gispert JD, Reig S, Pascau J, Vaquero JJ, Garcia-Barreno P, Desco M. Method for bias field correction of brain T1-weighted magnetic resonance images minimizing segmentation error. Hum Brain Mapp 2004;22:133–44.

[10] Pham DL, Prince JL. An adaptive fuzzy C-means algorithm for the image segmentation in the presence of intensity inhomogeneities. Pattern Recogn Lett 1998;20:57–68.

[11] Ahmed MN, Yamany SN, Mohamed N, Farag AA, Moriarty T. A modified fuzzy C-means algorithm for bias field estimation and segmentation of MRI data. IEEE Trans Med Imaging 1998;22(3): 57–68.

[12] Manjon JV, Lull JJ, Carbonell-Caballero J, Garcia-Marti G, Marti-Bonmari L, Robles M. A nonparametric MRI inhomogeneity correction method. Med Image Anal 2007;11:336–45.

[13] Ridler TW, Calvard S. Picture thresholding using an iterative selection method. IEEE Trans Syst Man Cybern 1978;8:630–2.

[14] Broyden CG. The convergence of a class of double-rank minimization algorithms. J Inst Math Appl 1970;6:76–90.

[15] Sled JG, Zijdenbos AP, Evans AC. A nonparametric method for automatic correction of intensity nonuniformity in MRI data. IEEE Trans Med Imaging 1998;17(1):87–97.

[16] Sijbers J, den Dekker AJ, Scheunders P, Van Dyck D. Maximum likelihood estimation of Rician distribution parameters. IEEE Trans Med Imaging 1998;17(3):357–61.

[17] Cocosco CA, Kollokian V, Kwan RS, Evans AC. Brainweb: Online interface to a 3D MRI simulated brain database; http://www.bic.mni. mcgill.ca/brainweb/. NeuroImage 1997;5(4):S425.